

A statistical reconstruction algorithm for positronium lifetime imaging using time-of-flight positron emission tomography

Hsin-Hsiung Huang, Zheyuan Zhu, Slun Booppasiri, Zhuo Chen, Shuo Pang, and Chien-Min Kao

Abstract—Positron emission tomography (PET) is an important modality for diagnosing diseases such as cancer and Alzheimer’s disease, capable of revealing the uptake of radiolabeled molecules that target specific pathological markers of the diseases. Recently, positronium lifetime imaging (PLI) that adds to traditional PET the ability to explore properties of the tissue microenvironment beyond tracer uptake has been demonstrated with time-of-flight (TOF) PET and the use of non-pure positron emitters. However, achieving accurate reconstruction of lifetime images from data acquired by systems having a finite TOF resolution still presents a challenge. This paper focuses on the two-dimensional PLI, introducing a maximum likelihood estimation (MLE) method that employs an exponentially modified Gaussian (EMG) probability distribution that describes the positronium lifetime data produced by TOF PET. We evaluate the performance of our EMG-based MLE method against traditional approaches using exponential likelihood functions and penalized surrogate methods. Results from computer-simulated data reveal that the proposed EMG-MLE method can yield quantitatively accurate lifetime images. We also demonstrate that the proposed MLE formulation can be extended to handle PLI data containing multiple positron populations.

Index Terms—Positron emission tomography, time-of-flight, positronium lifetime imaging, maximum likelihood.

I. INTRODUCTION

Positronium lifetime imaging (PLI) with time-of-flight (TOF) positron emission tomography (PET) represents a recent advancement in medical imaging, with its feasibility substantiated through various experimental studies [1]–[5]. Traditional PET is known for assessing the functional state of organs or tissues through the uptake of specific PET molecules. In contrast, PLI aims to measure the lifetime of positronium that is a meta-stable electron-positron pair formed by the positrons emitted by PET molecules [6]. More precisely, it measures the lifetime of so-called ortho-positronium (o-P) that can be significantly affected by the interaction of an o-P with nearby molecules, such as oxygen, that possess an unpaired electron. As a result, o-P lifetime can serve as a quantitative marker of such molecular presences in the tissue microenvironment, independent of the traditional PET molecule uptake mechanisms. This capability can be significant in clinical contexts.

This work did not involve human subjects or animals in its research.

This work was partially supported by NSF grant DMS-1924792 (Huang), DMS-2318925 (Huang) and NIH grant R01-EB029948 (Kao). Corresponding author: Hsin-Hsiung Huang.

Z. Zhu and S. Pang are with CREOL, The College of Optics and Photonics, University of Central Florida, Orlando, FL 32816 (e-mails: zyzhu@knights.ucf.edu, pang@ucf.edu)

C.-M. Kao is with Department of Radiology, University of Chicago, Chicago, IL 60637 (e-mail: ckao95@uchicago.edu).

Z. Chen is with Department of Mathematics, University of Arizona, Tucson, AZ 85721 (e-mail: zchen1@math.arizona.edu).

S. Booppasiri (email: slun.booppasiri@ucf.edu) and H.-H. Huang are with Department of Statistics and Data Science, University of Central Florida, Orlando, FL 32816 (email: hsin.huang@ucf.edu)

For instance, it may be used to identify hypoxic tissues that are often resistant to therapies [4], [7], potentially enabling enhanced treatment strategies for conditions like cancer.

Current experimental implementations of PLI ensure distinct separation of events based on their spatial origins [8], [9]. However, today’s TOF-PET systems, which have a coincidence resolving time (CRT) ranging from 200 to 600 ps full width at half maximum (FWHM) [10]–[12], have a spatial uncertainty of approximately 3–9 cm. Accurate image reconstruction of PLI data acquired by TOF-PET systems having a finite CRT presents a new challenge.

The inverse Laplace transform method [13] has been improved to separate various components in a lifetime histogram; it can substantially decrease the information loss commonly encountered when averaging lifetime data. This method does not perform image reconstruction. A few image reconstruction methods for PLI with TOF-PET have been recently reported [14]–[18]. A penalized surrogate (PS) method developed by Qi and Huang [14] for producing regularized maximum likelihood (ML) solution. Their model is based on a single-exponential probabilistic model for the PLI data that do not account for the effects of finite CRT to lifetime measurement. This paper introduces a refined statistical model for 2-dimensional TOF-PET PLI data, and an new algorithm that employs the Limited-memory Broyden-Fletcher-Goldfarb-Shanno Bound (L-BFGS-B) method from `scipy.optimize` [19], imposing nonnegativity condition for the solution.

The remainder of this paper is organized as follows: Section II details the formulation of the statistical model for the PLI list-mode data and the derivation of an algorithm to obtain the maximum likelihood estimates of lifetime images. Section III describes the computer-simulation study and presents the results. Section IV offers a summary and conclusions.

II. STATISTICAL MODEL FOR TOF-PET PLI DATA

A. Detection of a PLI event with TOF-PET

Figure 1 illustrates a two-dimensional (2D) TOF-PET system comprising a ring of uniformly spaced detectors that are numerically labeled by an integer i . It is assumed that a non-pure positron-emitter such as Sc-44, which emits a positron and a gamma ray effectively at the same time (called a prompt gamma), is employed. Compared to the popular PET isotopes like F-18, many non-pure positron-emitters have a larger positron range¹ that can limit the resulting image resolution [21]–[23]. In this work, we shall neglect positron range for it does not affect the fundamental validity of the proposed reconstruction method [14]. Similarly, photon acolinearity is also neglected [24].

¹Na-22 is a notable exception. See [20].

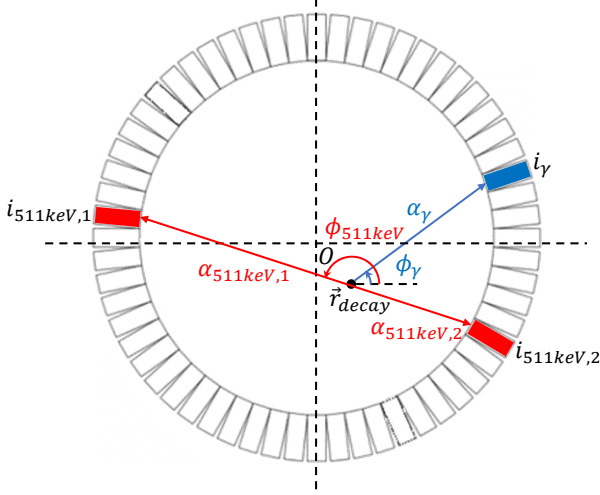


Fig. 1: Detection of a PLI event using a 2D TOF-PET system.

The decay of an isotope like Sc-44 releases a prompt gamma and a positron at location \mathbf{r}_{decay} and time t_{decay} . As illustrated in Figure 1, the prompt gamma travels a distance α_γ towards the detector ring at angle ϕ_γ , captured by detector i_γ at time $t_\gamma = t_{decay} + \alpha_\gamma/v_c$ where v_c is the speed of light. The positron can momentarily form a positronium before it annihilates with an electron. The elapse time before annihilation τ is described by an exponential distribution [8], given by

$$p(\tau; \lambda) = \text{Exp}(\tau; \lambda) = \begin{cases} \lambda e^{-\lambda \tau} & \tau \geq 0 \\ 0 & \tau < 0. \end{cases} \quad (1)$$

Lifetime refers to the inverse of the rate constant λ ; these two terms will be used interchangeably in this paper. There are, in fact, two positronium populations: para-positronium (p-P) and ortho-positronium (o-P). Positrons that do not form positroniums before annihilation, called direct annihilation (DA), also can exist for a finite time. The DA and p-P lifetimes are substantially shorter than the o-P lifetime. Unlike the o-P lifetime, the DA and p-P lifetimes, and the proportions of the DA, p-P and o-P populations, are not sensitive to the environment. Therefore, the main interest in PLI is the o-P lifetimes. Please see [4], [8] for in-depth discussion.

On annihilation, as depicted by the red line in the Fig. 1, two opposite 511 keV gamma rays are created. They travel from \mathbf{r}_{decay} at a random angle ϕ_{511keV} with respect to ϕ_γ and are detected by detectors $i_{511keV,1}$ and $i_{511keV,2}$ at time $t_{511keV,1} = t_{decay} + \tau + \alpha_{511keV,1}/v_c$ and $t_{511keV,2} = t_{decay} + \tau + \alpha_{511keV,2}/v_c$ respectively, where $\alpha_{511keV,1}$ and $\alpha_{511keV,2}$ are the distances that they travel.

The conventional TOF-PET system reports $i_{511keV,1}$, $i_{511keV,2}$, and the TOF given by

$$\Delta t_{511keV} = t_{511keV,1} - t_{511keV,2} = (\alpha_{511keV,1} - \alpha_{511keV,2})/v_c. \quad (2)$$

We assume that the system is extended to be capable of triple-coincidence detection and reports additionally i_γ and

$$\begin{aligned} \Delta t_\gamma &= (t_{511keV,1} + t_{511keV,2})/2 - t_\gamma \\ &= \tau + (\alpha_{511keV,1} + \alpha_{511keV,2} - 2\alpha_\gamma)/(2v_c). \end{aligned} \quad (3)$$

Note that $\alpha_{511keV,1} + \alpha_{511keV,2}$ can be determined from the locations of detectors $i_{511keV,1}$ and $i_{511keV,2}$. Additionally, if Δt_{511keV} is precisely known, \mathbf{r}_{decay} can be identified, and then α_γ can be computed from i_γ and \mathbf{r}_{decay} . Then, Eq. (3) can be used to compute τ from Δt_γ .

In a real system, the time measurement has limited precision and is typically binned and stored as integers. CRT refers to the uncertainty of Δt_{511keV} in FWHM. With a finite CRT, \mathbf{r}_{decay} cannot be precisely determined. A CRT of 200 ps to a 600 ps translates to an uncertainty of 3 cm to 9 cm in \mathbf{r}_{decay} . Similarly, Δt_γ will have limited precision and be binned. Hence, in Eq. (3) α_γ is not precisely observed and all the time measurements involved contain statistical variations.

B. Probability model for the TOF-PET PLI list-mode data

In conventional PET, data is associated with a line of response (LOR) $\mathcal{L}(i_{511keV,1}, i_{511keV,2})$ connecting two detectors $i_{511keV,1}$ and $i_{511keV,2}$ that capture the annihilation photons. TOF-PET refines this by segmenting each LOR based on the binned TOF value, creating non-overlapping segments referred to as lines of segment (LOS). Each LOS is identified by a multi-index $c = (i_{511keV,1}, i_{511keV,2}, m)$, indicating the specific TOF bin m on the LOR. We assume that the PLI events are given by $w = (c, i_\gamma, \Delta t_\gamma)$, where c identifies the LOS, i_γ is the detector that captures the prompt gamma, and Δt_γ is the time difference between the detection of the annihilation photons and the prompt gamma. These PLI events are stored as list-mode (LM) data, represented as $\mathcal{W}_{N_k} = \{w_k\}_{k=1}^{N_k}$, where k indexes a list of event words $w_k = (c_k, i_{\gamma,k}, \Delta t_{\gamma,k})$ and N_k is the total number of events.

1) *Calculation of the system matrix:* Each element $H_{c,j}$ of the system matrix \mathbf{H} is designed to reflect the likelihood that an annihilation taking place in image pixel j results in a detection at LOS c . The system matrix is calculated using a ray-tracing method [25], identifying which pixels are intersected by $\mathcal{L}(i_{511keV,1}, i_{511keV,2})$ and measuring their boundaries. A Gaussian function, whose width is given by the CRT, is centered at the midpoint of these boundaries for each intersecting pixel j' . The integral of this Gaussian over each TOF bin yields the values for $H_{(i_{511keV,1}, i_{511keV,2}, m), j'}$, using $(2/\sqrt{\pi}) \int_a^b e^{-t^2} dt = \text{erf}(b) - \text{erf}(a)$, where $\text{erf}(x)$ is the error function. Pixels not intersected by the LOS are assigned a zero value in the system matrix.

2) *Maximum likelihood estimation:* Let the vectors $\mathbf{f} = [f_j]$ and $\boldsymbol{\lambda} = [\lambda_j]$ be, respectively, the activity and o-P rate-constant images, where $f_j \geq 0$ and $\lambda_j \geq 0$ are their respective values in voxel j . τ_k can be computed from c_k , $i_{\gamma,k}$, and $\Delta t_{\gamma,k}$ to produce the LM data set $\mathcal{W}_{N_k}^0 = \{w_k^0\}_{k=1}^{N_k}$ with $w_k^0 = (c_k, \tau_k)$ in place of \mathcal{W}_{N_k} . We will derive in the Appendix that the log-likelihood for $\boldsymbol{\lambda}$ given \mathbf{f} and $\mathcal{W}_{N_k}^0$ is

$$\ell(\boldsymbol{\lambda}; \mathbf{f}, \mathcal{W}_{N_k}^0) = \sum_{k=1}^{N_k} \log \left(\sum_{j=1}^{N_j} H_{c_k, j} f_j \text{EMG}(\tau_k; \lambda_j, \sigma^2) \right), \quad (4)$$

where $\text{EMG}(\tau; \lambda, \sigma^2)$, the exponentially modified Gaussian (EMG) distribution, is the convolution of $\text{Exp}(\tau; \lambda)$ with a

zero-mean Gaussian with standard deviation σ that is introduced to take in account the uncertainty in measurement of τ . The convolution can be explicitly evaluated to yield [26]:

$$\text{EMG}(\tau; \lambda, \sigma^2) = \frac{1}{2} \lambda e^{-\lambda(\tau - \frac{1}{2}\sigma^2\lambda)} \left(1 + \text{erf} \left(\frac{\tau - \lambda\sigma^2}{\sqrt{2}\sigma} \right) \right), \quad (5)$$

where $\text{erf}(x)$ is the error function. It can be checked that $\text{EMG}(\tau; \lambda, 0) = \text{Exp}(\tau; \lambda)$

Note that the TOF-PET PLI LM data contains the traditional TOF-PET LM data $\mathcal{C}_{N_k} = \{c_k\}_{k=1}^{N_k}$. Approaches for solving \mathbf{f} from \mathcal{C}_{N_k} , and from histogram-mode data derived from it, are well established [citation]. A popular algorithm is the ordered-subsets (OS) expectation-maximization (EM) algorithm [27] that is an accelerated version of the EM algorithm for PET image reconstruction that can produce maximum-likelihood estimation (MLE) for \mathbf{f} . In this paper, we will employ the OS-EM algorithm for estimation of \mathbf{f} . The MLE of λ is then obtained by maximizing $\ell(\lambda; \mathbf{f}, \mathcal{W}_{N_k}^0)$ given in Equation (4) by using either the true \mathbf{f} or its estimate $\hat{\mathbf{f}}$ obtained by OS-EM. Maximization is carried out by using the Limited-memory Broyden-Fletcher-Goldfarb-Shanno Bound (L-BFGS-B) method available from `scipy.optimize` [19]. Positivity condition on λ is implemented but no explicit noise regularization schemes are introduced.

III. COMPUTER-SIMULATION STUDIES

We generated the TOF-PET PLI LM data, \mathcal{W}_{N_k} , using Monte Carlo methods tailored for a scanner configuration with N_{det} detectors uniformly distributed on a diameter D . Given \mathbf{f} and λ , we simulated the decay process as follows.

First, given a desired number of total decays, the image \mathbf{f} was scaled such that its pixel values represented the desired mean number of decays. Then, a list of decays was sampled from a Poisson distribution defined by these means. For each decay, its position, $\mathbf{r}_{decay} = (x_{decay}, y_{decay})^T$, was sampled within the bounds of the selected pixel area $A_j = [x_j - \Delta x/2, x_j + \Delta x/2] \times [y_j - \Delta y/2, y_j + \Delta y/2]$, where (x_j, y_j) represented the center coordinates of pixel j , and Δx and Δy were the pixel dimensions along the x and y axes, respectively, according to a uniform distribution, \mathcal{U}_{A_j} .

Then, a prompt gamma emitted in a random angle ϕ_γ , sampled from $\mathcal{U}[0, 2\pi)$, was generated at \mathbf{r}_{decay} . The travel distance α_γ before detection was determined by solving:

$$|\mathbf{r}_{decay} + \alpha_\gamma \hat{\phi}| = D/2, \quad (6)$$

where $\hat{\phi} = (\cos \phi, \sin \phi)^T$ is the unit direction vector. This equation has two solutions given by

$$\alpha_\gamma^\pm = -\hat{\phi}_\gamma^T \mathbf{r}_{decay} \pm \sqrt{(\hat{\phi}_\gamma^T \mathbf{r}_{decay})^2 - \|\mathbf{r}_{decay}\|^2 + D^2/4}, \quad (7)$$

due to uniform sampling of ϕ_γ the solution α_γ^+ can be arbitrarily used for consistency, yielding $\mathbf{r}_{detect, \gamma} = \mathbf{r}_{decay} + \alpha_\gamma^+ \hat{\phi}_\gamma$. The index i_γ of the detector that the prompt gamma hits was calculated by:

$$i_\gamma = \left\lfloor \left(\frac{N_{det}}{2\pi} \right) \angle \mathbf{r}_{detect, \gamma} \right\rfloor, \quad (8)$$

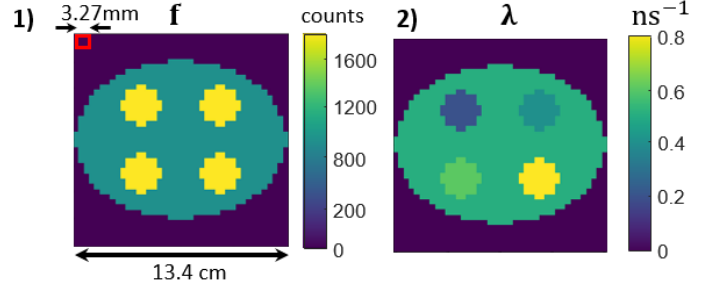


Fig. 2: Activity images (left column) and rate-constant images (right column) of Phantom 1. These images consists of $3.27 \times 3.27 \text{ mm}^2$ square pixels. Radius of each disc is 12 mm.

where $\angle \mathbf{r}$ denotes the angle of vector \mathbf{r} in polar coordinates, and $\lfloor x \rfloor$ represents the floor function.

Similarly, two opposing annihilation photons were emitted at \mathbf{r}_{decay} in a random angle ϕ_{511keV} sampled from $\mathcal{U}[0, 2\pi)$. The distances $\alpha_{511keV,1}$ and $\alpha_{511keV,2}$, and detector indices $i_{511keV,1}$ and $i_{511keV,2}$ were calculated as described above, now using both solutions in Eq. (7). The emission angles ϕ_γ and ϕ_{511keV} were independent.

The detection time $t_{511keV,1}$, $t_{511keV,2}$, and t_γ relative to the decay time t_{decay} were readily calculated from their travel distances, divided by v_c . To account for time-measurement uncertainty of the TOF-PET system, these time values were displaced by random amounts that were sampled from a Gaussian distribution $\mathcal{N}(0, \sigma^2)$, where $\sigma = \text{CRT}/2\sqrt{2\ln 2}$. The TOF was then calculated using $\Delta t_{511keV} = t_{511keV,1} - t_{511keV,2}$ and $\Delta t_\gamma = (t_{511keV,1} + t_{511keV,2})/2 - t_\gamma$. To reflect the practice in real systems, these time values are then binned, using a binsize of $\text{CRT}/2$. The measured τ should be computed from Δt_γ by correcting for the travel-time difference between the prompt gamma and annihilation photons. This travel time difference can be estimated from $i_{511keV,1}$, $i_{511keV,2}$, i_γ , and Δt_{511keV} . For simplicity, in this work we used the exactly known travel distances and computed τ as:

$$\tau = \Delta t_\gamma - \frac{\alpha_{511keV,1} + \alpha_{511keV,2} - 2\alpha_\gamma}{2v_c}. \quad (9)$$

We generated TOF-PET PLI LM data with $N_{det} = 364$, $D = 57.2 \text{ cm}$, and a CRT of 400ps, using nineteen 200ps-width time bins. These settings resulted in approximately 2.52 million TOF-PET channels. Our simulations considered only valid triple-coincidence events. Attenuation, scattering, and random events were not included. To evaluate our proposed reconstruction method, two numerical phantoms were considered. The rate-constant image of Phantom 1, shown in Fig. 2, has four discs (radii = 12mm) with different λ values (0.2, 0.4, 0.6, and 0.8 ns^{-1}) on top of a circular background hat has a rate constant of 0.5 ns^{-1} . Pixel index (x, y) is used for identifying the center location of each insert. The pixel index of upper left, upper right, lower left and lower right regions are (13.5, 14.5), (28.5, 14.5), (13.5, 27.5), and (28.5, 27.5) respectively. Phantom 2 shown in Fig. 6 has the activity image that features an elliptical background enclosing two discs. Each pixel in these discs records twice

the number of decay events compared to those in the elliptical background. The decay-rate image for o-Ps includes two discs with different decay constants, λ (0.4 and 0.6 ns⁻¹), in contrast to the background ellipse with $\lambda = 0.5$ ns⁻¹. All phantoms, and the reconstruction images, contained 41×41 square pixels measuring 3.27×3.27 mm². The expected total number of events to generate was 1 million, and the initial estimate for $\hat{\lambda}$ was a uniform image of 0.5 ns⁻¹. Below, the proposed method is referred to as EMG-MLE. When $\sigma = 0$, the EMG distribution reduces to the Exp distribution; for distinction, the method will be referred to as Exp-MLE.

IV. RESULTS

The proposed reconstruction method will be compared with the penalized surrogate (PS) method developed by Qi and Huang [14], which iteratively updates an estimate for λ by:

$$\hat{\lambda}_j^{(m+1)} = \frac{\sum_{k=1}^{N_k} u_{c_{k,j}}^{(m)}}{\beta_j^m + \sum_{k=1}^{N_k} u_{c_{k,j}}^{(m)} \tau_k}, \quad (10)$$

where m is the iteration number,

$$u_{c_{k,j}}^{(m+1)} = \frac{H_{c_{k,j}} \hat{f}_j \lambda_j^{(m)} \exp(-\tau_k \times \lambda_j^{(m)})}{\sum_{l=1}^{N_j} H_{c_{k,l}} \hat{f}_l \lambda_l^{(m)} \exp(-\tau_k \times \lambda_l^{(m)})}, \quad (11)$$

and $\beta_j^m = \eta_j^m \beta$ where $\beta \geq 0$ is a regularization parameter and η_j^m is calculated from neighbors of pixel j to adjust the strength of regularization locally.

Given an image \mathbf{x} , the SALR is defined as [28], [29]:

$$\text{SALR}(\mathbf{x})_p = \frac{|\log(\mathbf{x}_p / \mathbf{x}_b)|}{\text{SD}(\mathbf{x}_b) / \bar{\mathbf{x}}_b}, \quad (12)$$

where $\bar{\mathbf{x}}$ and $\text{SD}(\mathbf{x})$ are the average and standard deviation over pixels in \mathbf{x} , \mathbf{x}_p contains pixels of \mathbf{x} in a region of interest (ROI) p , and \mathbf{x}_b contains pixels of \mathbf{x} in the surrounding background of the ROI. As detailed in [28], higher SALR values are desired because it measures the contrast of an ROI against the background variability due to noise. Therefore, unless mentioned otherwise, for EMG-MLE, Exp-MLE and PS we calculate an overall SALR by averaging $\text{SALR}(\hat{\lambda})_p$, where $p =$ is a number identifies a disc in the phantoms, and select the iteration number that yields the largest overall SALR.

A. Activity and decay rate constant reconstruction

Figure 3 illustrates the outcomes from various reconstruction methods applied to Phantom 1. The subfigures (1 & 2) show the rate-constant images, $\hat{\lambda}_{\text{EMG-MLE}}$ and $\hat{\lambda}_{\text{Exp-MLE}}$, obtained by EMG-MLE and Exp-MLE, respectively. Subfigures (3 & 4) display the results of PS method, using $\beta = 0$ and 10. In these reconstructions, the true isotope image \mathbf{f} is used. The differences between these images are not readily apparent.

Figure 4, on the other hand, compares the rate-constant images obtained by various reconstruction methods when using $\hat{\mathbf{f}}$ produced from simulated data using the OS-EM algorithm. With $\hat{\mathbf{f}}$, although the activity is low in the area external to the phantom, it does not vanish. As a result, unlike those shown in Figure 3, the external area of the resulting rate-constant images is not zero. In EMG-MLE, the external

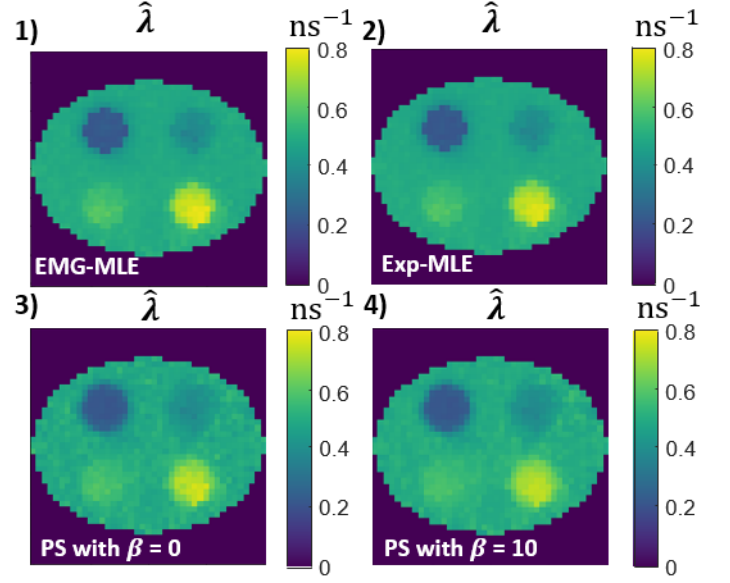


Fig. 3: Results obtained for Phantom 1. (1 & 2) $\hat{\lambda}_{\text{EMG-MLE}}$ and $\hat{\lambda}_{\text{Exp-MLE}}$ produced by EMG-MLE and Exp-MLE. (3 & 4) $\hat{\lambda}_{\text{PS}}$ produced by the penalized surrogate method [14] with $\beta = 0$ and 10. The true \mathbf{f} is used in these reconstructions.

area remains at its initial value, which happens to be equal to the background circle (0.5 ns⁻¹). In PS, significant streaks occur when using $\beta = 0$ (no regularization) and they can be removed when using $\beta = 10$. Based on the profiles in Figure 4 (5) and (6), the upper discs of the EMG-MLE are comparable, while the lower discs are closer to the true values than those in the PS images.

To quantitatively evaluate the reconstruction accuracy, we considered the normalized mean square error (NMSE), defined as:

$$\text{NMSE} = \frac{\|\hat{\lambda} - \lambda\|^2}{\|\lambda\|^2}, \quad (13)$$

where $\|\cdot\|$ denotes the Euclidean norm. We computed pixel-wise means and standard deviations of the NMSE of the images reconstructed from ten independent simulations, using EMG-MLE, Exp-MLE, and PS with $\beta = 0, 5, 10$. Then we obtained the average mean and standard deviation inside various regions, including the four discs and the background circle excluding the discs. The results, summarized in Supplementary Table S1 and illustrated as boxplots in Figure 5, demonstrate that EMG-MLE achieves lower NMSE means, or at least comparable to those of PS, particularly for the upper-left disc, the lower-right disc, and the background. Most standard deviations given by EMG-MLE are less than those by PS. Notably, when using the true \mathbf{f} in EMG-MLE achieves only slightly lower average NMSE means and standard deviations than when using the estimated $\hat{\mathbf{f}}$. This suggests stability of EMG-MLE with respect to noise even though no explicitly noise regularization scheme is incorporated.

We also conduct cross-correlation analysis to quantify potential cross-talk between the activity map used and the

Regions	Correlation				
	EMG-MLE	Exp-MLE	PS $\beta = 0$	PS $\beta = 5$	PS $\beta = 10$
Upper left	1.20×10^{-1} (5.91×10^{-3})	1.23×10^{-1} (8.39×10^{-3})	1.43×10^{-1} (8.23×10^{-3})	1.41×10^{-1} (8.57×10^{-3})	1.41×10^{-1} (9.02×10^{-3})
Upper right	-6.14×10^{-4} (5.39×10^{-3})	2.64×10^{-3} (7.58×10^{-3})	1.11×10^{-2} (3.40×10^{-3})	9.45×10^{-3} (4.35×10^{-3})	8.13×10^{-3} (4.47×10^{-3})
Lower left	-6.72×10^{-2} (5.90×10^{-3})	-7.08×10^{-2} (5.94×10^{-3})	-7.09×10^{-2} (5.41×10^{-3})	-7.38×10^{-2} (6.36×10^{-3})	-7.78×10^{-2} (5.98×10^{-3})
Lower right	-1.20×10^{-1} (5.17×10^{-3})	-1.29×10^{-1} (4.07×10^{-3})	-1.41×10^{-1} (3.37×10^{-3})	-1.44×10^{-1} (8.49×10^{-3})	-1.49×10^{-1} (9.31×10^{-3})
Background	-2.73×10^{-2} (1.85×10^{-3})	-2.94×10^{-2} (1.62×10^{-3})	-3.21×10^{-2} (1.99×10^{-3})	-2.47×10^{-2} (1.90×10^{-3})	-1.53×10^{-2} (1.93×10^{-3})

TABLE I: Comparisons of the cross-correlations using the five methods for Phantom 1 using $\hat{\mathbf{f}}$. The SD is shown in the parenthesis.

resulting $\hat{\boldsymbol{\lambda}}$. The cross-correlation is defined as:

$$C := \frac{(\hat{\boldsymbol{\lambda}} - \boldsymbol{\lambda})^T \cdot \mathbf{f}}{\|\boldsymbol{\lambda}\| \|\mathbf{f}\|}. \quad (14)$$

The low cross-correlation values reported in Table I indicate negligible interactions from \mathbf{f} into $\hat{\boldsymbol{\lambda}}$.

These findings underscore the efficacy of EMG-MLE in accurately reconstructing rate-constant images from TOF-PET having a CRT of 400 ps.

B. Effects of CRT

To examine the potential effects of CRT on EMG-MLE, we performed reconstructions from simulated events with CRTs of 200, 400, 600 and 800 ps using Phantom 2 shown in Fig. 6. The true activity image \mathbf{f} was used.

The width of the time bin was selected to be equal to $\text{CRT}/2$. The total number of events to simulate was 3 million. For each CRT, ten independent Monte Carlo instances were generated. Fig. 7 shows the boxplot of the NMSE of the rate-constant images obtained using EMG-MLE and Exp-MLE. Here, the NMSE means and standard deviations are the average of the pixel-wise means and standard deviations over the entire phantom. Generally, in terms of the mean NMSE, the accuracy of both methods decreases as the CRT increases, and the EMG-MLE outperforms Exp-MLE. These may be explained by the fact that the uncertainty in τ_k and the discrepancy of the Exp model with the data increase with the CRT. However, for EMG-MLE and Exp-MLE, smaller mean values are obtained at 800 ps than at 600 ps. Also, the EMG-MLE yields slightly larger standard deviations at 600 ps and 800 ps than Exp-MLE. At present, we do not have explanations for these behaviors. Fig. 8 compares the horizontal profiles across the center of the two top discs of the ground truth $\boldsymbol{\lambda}$ map and the reconstructed images obtained by the EMG-MLE and Exp-MLE. These results demonstrate that EMG-MLE consistently achieves superior accuracy for all CRT values. Furthermore, Fig. 7 displays the NMSE obtained from 10 simulations across various CRTs using both EMG-MLE and Exp-MLE for the activity and lifetime maps in Fig. 6, showing that EMG-MLE consistently yields lower NMSE compared to Exp-MLE for different CRTs.

C. The presence of an additional constant decay component

Further comparisons of EMG-MLE and PS reconstructions are shown in Fig. 3. Additionally, the reconstruction accuracy of MLE using an Exponential distribution for the lifetime decays (Exp-MLE) and the proposed MLE using an Exponential modified Gaussian distribution for the lifetime decays (EMG-MLE) were assessed. Ten simulations for Phantom 2 were conducted for different CRTs ranging from 200 ps to 800 ps using 3 million PLI events and the estimated \mathbf{f} map, employing both EMG-MLE and Exp-MLE methods.

So far, we have considered only o-Pos. As already mentioned, substantially faster DA and p-P populations co-exist, and proportions of the DA, p-P and o-P populations, approximately equal to 0.6, 0.1, and 0.3, are not sensitive to the environment [8]. We extended our simulations to include two rate-constant images, $\boldsymbol{\lambda}_1$ for o-P and $\boldsymbol{\lambda}_2$ for DA, neglecting The p-P population for now due to its relatively population weight. As described in Appendix, in this case $\text{EMG}(\tau_k; \lambda_j, \sigma^2)$ in Eq. (4) will be replaced with

$$w_1 \text{EMG}(\tau_k; \lambda_{1,j}, \sigma^2) + w_2 \text{EMG}(\tau_k; \lambda_{2,j}, \sigma^2), \quad (15)$$

where $\lambda_{1,j}$ and $\lambda_{2,j}$ are the values of $\boldsymbol{\lambda}_1$ and $\boldsymbol{\lambda}_2$ at pixel j , respectively, and w_1 and w_2 with $w_1 + w_2 = 1$ are the population weights for o-P and DA events, respectively. The isotope image \mathbf{f} and the o-P rate-constant image $\boldsymbol{\lambda}_1$ remained those of Phantom 2. On the other hand, the DA rate-constant image $\boldsymbol{\lambda}_2$ was the background ellipse of the phantom taking the value of 2.5 ns^{-1} . Also, $w_1 = 0.3$ was used. A simulated data had an expected 3-million events. In reconstruction, the exactly known w_1 , \mathbf{f} , and $\boldsymbol{\lambda}_2$, were used for obtaining the MLE of $\boldsymbol{\lambda}_1$. More details about the two-population model can be found in [29].

Fig. 9 shows the reconstructed o-P rate-constant image of the single-population and two-population model for Phantom 2, using one million events and 400 ps CRT. The reconstructed image of the two-population model yields a higher contrast of two circular regions relative to the background compared to the single-population model. In addition, the single-population model fails to reconstruct the difference in the rate-constant value between the two circular regions. This preliminary experiment shows that the proposed method can be extended to handle multi-population data.

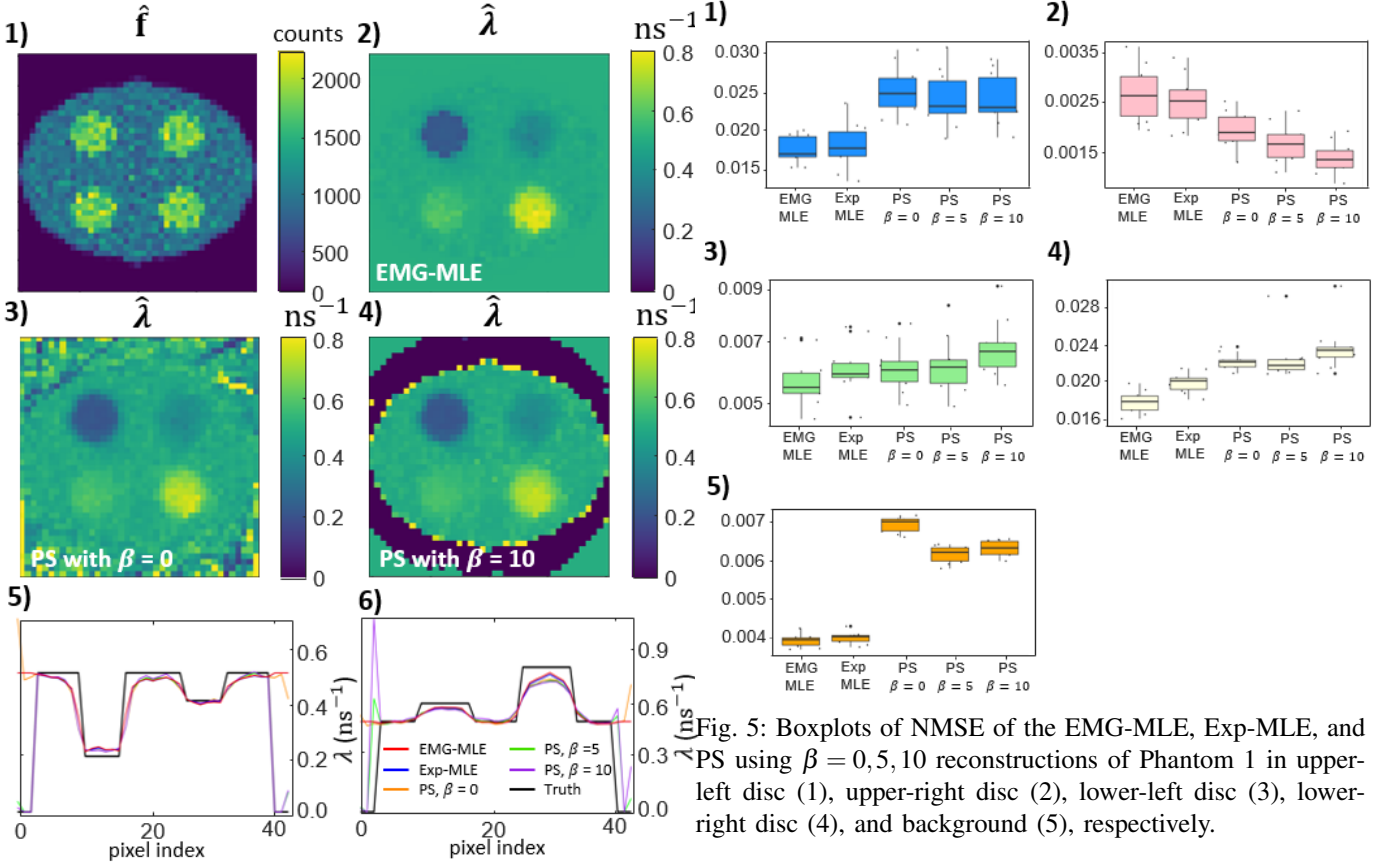


Fig. 4: Results obtained for Phantom 1. \hat{f} in panels 1) shows the isotope image reconstructed from simulated data using OS-EM. $\hat{\lambda}$ in panel 2), 3), and 4) are rate-constant images obtained, respectively, by EMG-MLE, PS with $\beta = 0$, and PS with $\beta = 10$ when using \hat{f} . Plots in 5) & 6) show horizontal profiles across the center of, respectively, the upper and lower discs of these reconstructed rate-constant images. For comparison, the true profiles and the profiles of rate-constant images obtained by Exp-MLE and PS with $\beta = 5$, using \hat{f} , are also shown.

V. SUMMARY AND DISCUSSIONS

In this study, we developed a maximum likelihood (ML)-based algorithm for reconstructing positronium lifetime images from list-mode data acquired by a TOF-PET system that is extended for detecting triple coincidences when a $\beta^+ + \gamma$ isotope such as Sc-44 is used. We conducted computer simulation studies for a 2-D TOF-PET system that emulates the configurations of human TOF-PET systems with 288 detectors on a 57 cm diameter ring. CRTs of 200 ps, 400 ps, 600 ps, and 800 ps are considered.

Our results demonstrate that the estimated rate-constant images $\hat{\lambda}_{\text{EMG-MLE}}$ or $\hat{\lambda}_{\text{Exp-MLE}}$ agree well with the ground truth. As CRT increases, the accuracy of both methods generally decreases, but EMG-MLE consistently outperforms Exp-MLE. Our method incorporates Gaussian blur into the likelihood function and can be extended to a two-population model (o-P and p-P), which distinguishes it from existing approaches.

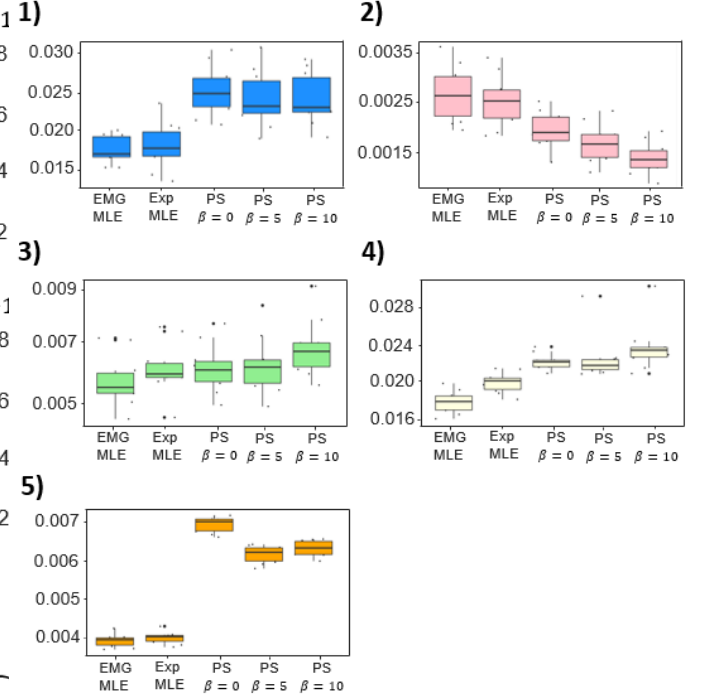


Fig. 5: Boxplots of NMSE of the EMG-MLE, Exp-MLE, and PS using $\beta = 0, 5, 10$ reconstructions of Phantom 1 in upper-left disc (1), upper-right disc (2), lower-left disc (3), lower-right disc (4), and background (5), respectively.

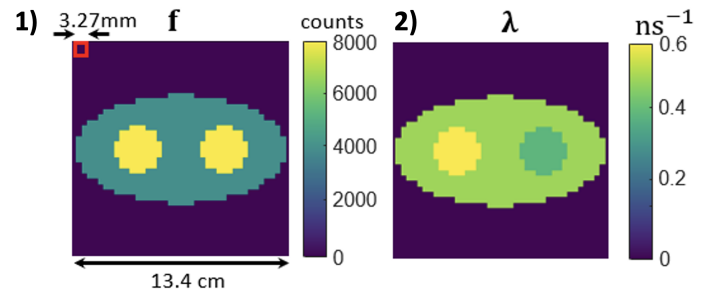


Fig. 6: The activity image (a) and the rate-constant image (b) of Phantom 2, with a pixel size of 3.27 mm. This phantom was used to examine the reconstruction method under different CRTs.

Our current studies have not accounted for attenuation, scatter, and random events. In addition, multiple lifetime populations are present and we have only preliminary extended the proposed method to include two populations (direct annihilation of positron with electron also is characterized by its own decay rate constant). Moving forward, we plan to extend our model to include these factors to fit real-world PLI data more accurately. Triple coincidences have a much lower probability of occurrence than the conventional annihilation coincidences. Although emerging systems such as the Total-Body systems can offer an adequate sensitivity [citation], we can expect the PLI data to be count limited, in general. Therefore, resolution-preserving noise regularization can be an important consideration in PLI reconstruction. Given the

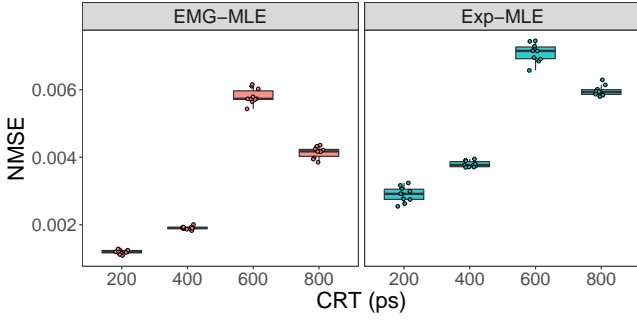


Fig. 7: The NMSEs of Phantom 2 as a function of CRT, for 3 million-event data.

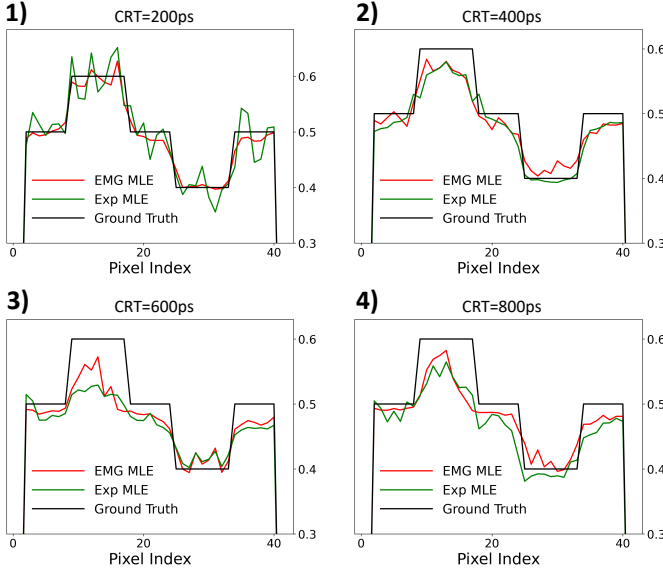


Fig. 8: The horizontal profiles through the center of images and the phantom for various CRTs for a single simulation run.

complexity, discrepancies between the model assumed for reconstruction and the data are very likely to exist. Another issue of practical significance is the computation complexity when extending the method to 3-D TOF-PET systems. Therefore, we also plan to delve into Bayesian modeling and regularized optimization, coupled with parallel computation strategies, to develop accurate, robust, and compute-efficient reconstruction

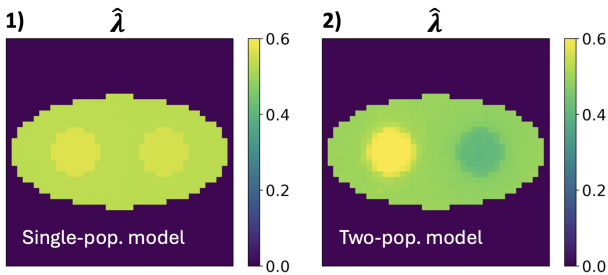


Fig. 9: o-P rate-constant image obtained by the single-population and two-population model for Phantom 2. 1) Single-population model. 2) Two-population model.

algorithms for PLI.

APPENDIX

In this appendix, we elaborate on the derivation of the joint likelihood for the PLI data acquired by using a TOF-PET system. Let $f_j \geq 0$ be the PET activity in pixel j so that the number of positrons released in pixel j during an interval T is a Poisson random number with mean $f_j T$. A released positron in pixel j can exist for a duration whose distribution following an exponential distribution $\text{Exp}(\tau; \lambda_j)$ with some $\lambda_j \geq 0$ before annihilation. Assume that the uncertainty in the measurement of τ is described by $g(\tau; 0, \sigma^2)$ – a zero-mean Gaussian with standard deviation σ , the distribution of the observed τ will be the convolution of $\text{Exp}(\tau; \lambda)$ with $g(\tau; 0, \sigma^2)$, which can be evaluated to yield the Exponentially Modified Gaussian $\text{EMG}(\tau; \lambda_j, \sigma^2)$ given in Eq. (5). Subsequently, annihilation of a positron produces two opposite 511 keV photons that may be detected by the TOF-PET system at an LOS, say $c = (i_{511\text{keV},1}, i_{511\text{keV},2}, m)$ where $i_{511\text{keV},1}$ and $i_{511\text{keV},2}$ are the indices of the detectors making the detection and m is the TOF index (the TOF value is typically binned). In this treatment, a PLI detection is given by (c, τ) .

Let $\mathbf{f} = [f_j]^T$ and $\boldsymbol{\lambda} = [\lambda_j]^T$ be vectors representing the activity and rate-constant images. Given a PLI detection, we denote by $p(c, \tau | \boldsymbol{\lambda}, \mathbf{f}) d\tau$ the probability for it to be in the set $S_{d\tau}(c, \tau) = \{(c, \tau') : \tau \leq \tau' < \tau + d\tau\}$ when the activity and rate-constant image are \mathbf{f} and $\boldsymbol{\lambda}$, respectively. Evidently, $p(c, \tau | \boldsymbol{\lambda}, \mathbf{f}) d\tau$ equals to the ratio of $n_1(S_{d\tau}(c, \tau))$, the expected number of detections in $S_{d\tau}(c, \tau)$, to n_2 , the expected total number of all detections. Evidently,

$$n_1(S_{d\tau}(c, \tau)) = \sum_{j=1}^{N_j} f_j T \times \text{EMG}(\tau; \lambda_j, \sigma^2) d\tau \times H_{c,j}, \quad (16)$$

where $f_j T$ gives the expected number of positrons in pixel j , $\text{EMG}(\tau; \lambda_j, \sigma^2) d\tau$ gives the probability for one of these positrons to exist for a duration $\tau' \in [\tau, \tau + d\tau)$, and $H_{c,j}$ gives the probability for an annihilation in pixel j to yield a detection at LOS c . Here we have two made two assumptions: (i) the isotope decay, positron annihilation, and coincidence detection in a chain leading to a PLI detection are independent processes, and (ii) the processes involved in different PLI detections are independent. n_2 is the totality of $n_1(S_{d\tau}(c, \tau))$ over all possible c and τ :

$$n_2 = \sum_c \int_{\tau} S_{d\tau}(c, \tau) d\tau = T s_f, \quad (17)$$

where $s_f = \sum_{c,j} H_{c,j} f_j$. Therefore,

$$p(c, \tau | \boldsymbol{\lambda}, \mathbf{f}) = \frac{1}{d\tau} \frac{n_1}{n_2} = \frac{\sum_{j=1}^{N_j} H_{c,j} f_j \text{EMG}(\tau; \lambda_j, \sigma^2)}{s_f}. \quad (18)$$

Note that $p(c, \tau | \boldsymbol{\lambda}, \mathbf{f})$ is a probability in c but a density in τ .

Under independence assumptions, given N_k detections the probability for them to be $(c_1, \tau_1), \dots, (c_{N_k}, \tau_{N_k})$ is therefore $p(\mathcal{W}_{N_k}^0; \boldsymbol{\lambda}, \mathbf{f}) = \prod_{k=1}^{N_k} p(c_k, \tau_k | \boldsymbol{\lambda}, \mathbf{f})$, where $\mathcal{W}_{N_k}^0 = \{(c_k, \tau_k) : 1 \leq k \leq N_k\}$. Consequently, we have the log-likelihood

$$\ell(\boldsymbol{\lambda}, \mathbf{f}; \mathcal{W}_{N_k}^0) = \sum_{k=1}^{N_k} \log \left(\sum_{j=1}^{N_j} H_{c_k,j} f_j \text{EMG}(\tau_k; \lambda_j, \sigma^2) \right) - N_k \log(s_f). \quad (19)$$

Above we consider preset-count (PC) acquisition in which a scan is stopped when reaching a prescribed number N_k of detection. Alternatively, in preset-time (PT) acquisition a scan is conducted for a prescribed duration T and hence N_k becomes a Poisson random number with mean $n_2 = Ts_f$. With PT acquisition, the probability for having N_k detections and they are given by $\mathcal{W}_{N_k}^0$ is then $p'(\mathcal{W}_{N_k}^0; \mathbf{f}, \boldsymbol{\lambda}, T) = \text{Poisson}(N_k; Ts_f) \times p(\mathcal{W}_{N_k}^0; \boldsymbol{\lambda}, \mathbf{f})$, yielding the log-likelihood (omitting constants):

$$\ell'(\boldsymbol{\lambda}, \mathbf{f}; \mathcal{W}_{N_k}^0, T) = \sum_{k=1}^{N_k} \log \left(\sum_{j=1}^{N_j} H_{c_k,j} f_j \text{EMG}(\tau_k; \lambda_j, \sigma^2) \right) - Ts_f. \quad (20)$$

If \mathbf{f} is known *a priori*, the 2nd terms of these log-likelihoods are constants. Therefore, omitting constants both acquisition modes have the same profile log-likelihood given \mathbf{f} :

$$\ell(\boldsymbol{\lambda}; \mathcal{W}_{N_k}^0, \mathbf{f}) = \sum_{k=1}^{N_k} \log \left(\sum_{j=1}^{N_j} H_{c_k,j} f_j \text{EMG}(\tau_k; \lambda_j, \sigma^2) \right). \quad (21)$$

The gradient of $\ell(\boldsymbol{\lambda}; \mathcal{W}_{N_k}^0, \mathbf{f})$ is provided to the L-BFGS-B algorithm to speed up computation. It is an exercise to show

$$\frac{\partial \ell(\boldsymbol{\lambda}; \mathbf{f}; \mathcal{W}_{N_k}^0)}{\partial \lambda_j} = \sum_{k=1}^{N_k} \frac{H_{c_k,j} f_j \text{dEMG}(\tau_k; \lambda_j, \sigma^2)}{\sum_{j'=1}^{N_j} H_{c_k,j'} f_{j'} \text{EMG}(\tau_k; \lambda_{j'}, \sigma^2)}, \quad (22)$$

where

$$\begin{aligned} \text{dEMG}(\tau; \lambda, \sigma^2) &= \partial \text{EMG}(\tau; \lambda, \sigma^2) / \partial \lambda \\ &= \frac{1}{2} e^{-\lambda(\tau - \frac{1}{2}\sigma^2\lambda)} \left\{ -\frac{\sigma\lambda}{\sqrt{2\pi}} \exp^{-(\tau - \sigma^2\lambda)^2/2\sigma^2} \right. \\ &\quad \left. + (1 - \lambda\tau + \sigma^2\lambda^2) \left(1 + \text{erf} \left(\frac{\tau - \lambda\sigma^2}{\sqrt{2}\sigma} \right) \right) \right\}. \end{aligned} \quad (23)$$

As described in [2], positrons in fact can exist in multiple different states before annihilation, each of which is characterized by a distinct rate constant. In general, multiple rate-constant images, say $\boldsymbol{\lambda}_p$, $p = 1, \dots, N_p$, are therefore needed, and the probability distribution for the observed τ becomes $\sum_p w_p \text{EMG}(\tau; \lambda_{p,j}, \sigma^2)$ where w_p 's with $\sum_p w_p = 1$, $w_p \geq 0$ are the proportions of positrons existing in respective "population" (we shall assume that the population weights do not vary over pixels) and $\lambda_{p,j}$ is the value of $\boldsymbol{\lambda}_p$ at pixel j . Following the above derivation, the profile log-likelihood given \mathbf{f} is

$$\begin{aligned} \ell(w_1, \boldsymbol{\lambda}_1, \dots, w_{N_p}, \boldsymbol{\lambda}_{N_p}; \mathcal{W}_{N_k}^0, \mathbf{f}) \\ = \sum_{k=1}^{N_k} \log \left(\sum_{j=1}^{N_j} H_{c_k,j} f_j \sum_{p=1}^{N_p} w_p \text{EMG}(\tau_k; \lambda_{p,j}, \sigma^2) \right). \end{aligned} \quad (24)$$

In Section IV-C, we consider the case with $N_p = 2$ and treat w_1 , w_2 , and $\boldsymbol{\lambda}_2$ as constants, obtaining $\ell(\boldsymbol{\lambda}_1; w_1, w_2, \boldsymbol{\lambda}_2, \mathcal{W}_{N_k}^0, \mathbf{f})$. In this case, we need the gradient

$$\begin{aligned} \partial \ell(\boldsymbol{\lambda}_1; w_1, w_2, \boldsymbol{\lambda}_2, \mathcal{W}_{N_k}^0, \mathbf{f}) / \partial \lambda_{1,j} \\ = \sum_k \frac{H_{c_k,j} f_j w_1 \text{dEMG}(\tau_k; \lambda_{1,j}, \sigma^2)}{\sum_{j'} H_{c_k,j'} f_{j'} \sum_{p=1}^2 w_p \text{EMG}(\tau_k; \lambda_{p,j'}, \sigma^2)}. \end{aligned} \quad (25)$$

Although this paper does not consider simultaneous MLE of \mathbf{f} and $\boldsymbol{\lambda}$ using the joint log-likelihoods, several observations are worth noting. First, from Equation (19) it can be readily checked that $\ell(\boldsymbol{\lambda}, \xi \mathbf{f}; \mathcal{W}_{N_k}^0) = \ell(\boldsymbol{\lambda}, \mathbf{f}; \mathcal{W}_{N_k}^0)$ for any $\xi > 0$. This

reflects that, since PC acquisition does not care about the scan time, \mathbf{f} scanned for an interval ξT and $\xi \mathbf{f}$ scanned for an interval T are equal likely for explaining a given dataset. This observation leads us to stipulate that the log-likelihood maximizing \mathbf{f} for PC- and PT-acquisitions differ only in scale. To verify this, using Equations (19)&(20) we have

$$\ell'(\boldsymbol{\lambda}, \xi \mathbf{f}; \mathcal{W}_{N_k}^0) = \ell(\boldsymbol{\lambda}, \mathbf{f}; \mathcal{W}_{N_k}^0) + \alpha(\mathbf{f}, \xi), \quad (26)$$

where $\alpha(\mathbf{f}, \xi) = N_k \log(s_f) + N_k \log(\xi) - \xi T s_f$. One can readily check that, for any \mathbf{f} , $\alpha(\mathbf{f}, \xi)$ can reach its maximum value of $N_k \log(N_k/eT)$ by setting $\xi = N_k/Ts_f$. Therefore, if $(\mathbf{f}^*, \boldsymbol{\lambda}^*)$ maximizes $\ell(\boldsymbol{\lambda}, \mathbf{f}; \mathcal{W}_{N_k}^0)$, then $(\xi^* \mathbf{f}^*, \boldsymbol{\lambda}^*)$, $\xi^* = N_k/Ts_f$ maximizes $\ell'(\boldsymbol{\lambda}, \mathbf{f}; \mathcal{W}_{N_k}^0)$ because both terms on the right-hand side of Equation (26) are maximized. Consequently, it is sufficiently to consider only the PC joint log-likelihood $\ell(\boldsymbol{\lambda}, \mathbf{f}; \mathcal{W}_{N_k}^0)$. It is not difficult to see that the role of scaling by ξ^* is to fix the activity of a PC MLE solution to yield a PT MLE solution that best accounts for observation of N_k events during the prescribed scan time T .

REFERENCES

- [1] P. Moskal, D. Kisielewska, C. Curceanu, E. Czerwiński, K. Dulski, A. Gajos, M. Gorgol, B. Hiesmayr, B. Jasińska, K. Kacprzak *et al.*, "Feasibility study of the positronium imaging with the J-PET tomograph," *Physics in Medicine & Biology*, vol. 64, no. 5, p. 055017, 2019.
- [2] P. Moskal, B. Jasińska, E. Stepień, and S. D. Bass, "Positronium in medicine and biology," *Nature Reviews Physics*, vol. 1, no. 9, pp. 527–529, 2019.
- [3] P. Moskal, D. Kisielewska, R. Y. Shopa, Z. Bura, J. Chhokar, C. Curceanu, E. Czerwiński, M. Dadgar, K. Dulski, J. Gajewski *et al.*, "Performance assessment of the 2 γ positronium imaging with the total-body PET scanners," *EJNMMI physics*, vol. 7, no. 1, pp. 1–16, 2020.
- [4] K. Shibuya, H. Saito, F. Nishikido, M. Takahashi, and T. Yamaya, "Oxygen sensing ability of positronium atom for tumor hypoxia imaging," *Communications Physics*, vol. 3, no. 1, p. 173, 2020.
- [5] B. Zgardzińska, G. Chołubek, B. Jarosz, K. Wysogład, M. Gorgol, M. Goździuk, M. Chołubek, and B. Jasińska, "Studies on healthy and neoplastic tissues using positron annihilation lifetime spectroscopy and focused histopathological imaging," *Scientific Reports*, vol. 10, no. 1, p. 11890, 2020.
- [6] M. D. Harpen, "Positronium: Review of symmetry, conserved quantities and decay for the radiological physicist," *Medical Physics*, vol. 31, no. 1, pp. 57–61, 2004.
- [7] P. Moskal and E. Stepień, "Positronium as a biomarker of hypoxia," *Bio-Algorithms and Med-Systems*, vol. 17, no. 4, pp. 311–319, 2021.
- [8] P. Moskal, K. Dulski, N. Chug, C. Curceanu, E. Czerwiński, M. Dadgar, J. Gajewski, A. Gajos, G. Grudziński, B. C. Hiesmayr *et al.*, "Positronium imaging with the novel multiphoton PET scanner," *Science advances*, vol. 7, no. 42, p. eabh4394, 2021.
- [9] P. Moskal, A. Gajos, M. Mohammed, J. Chhokar, N. Chug, C. Curceanu, E. Czerwiński, M. Dadgar, K. Dulski, M. Gorgol *et al.*, "Testing cpt symmetry in ortho-positronium decays with positronium annihilation tomography," *Nature communications*, vol. 12, no. 1, p. 5658, 2021.
- [10] J. S. Karp, V. Viswanath, M. J. Geagan, G. Muehllehner, A. R. Pantel, M. J. Parma, A. E. Perkins, J. P. Schmall, M. E. Werner, and M. E. Daube-Witherspoon, "Pennpet explorer: design and preliminary performance of a whole-body imager," *Journal of Nuclear Medicine*, vol. 61, no. 1, pp. 136–143, 2020.
- [11] B. A. Spencer, E. Berg, J. P. Schmall, N. Omidvari, E. K. Leung, Y. G. Abdelhafez, S. Tang, Z. Deng, Y. Dong, Y. Lv *et al.*, "Performance evaluation of the uEXPLORER total-body PET/CT scanner based on NEMA NU 2-2018 with additional tests to characterize pet scanners with a long axial field of view," *Journal of Nuclear Medicine*, vol. 62, no. 6, pp. 861–870, 2021.
- [12] I. Alberts, J.-N. Hünermund, G. Prenosil, C. Mingels, K. P. Bohn, M. Viscione, H. Sari, B. Vollnberg, K. Shi, A. Afshar-Oromieh *et al.*, "Clinical performance of long axial field of view pet/ct: a head-to-head intra-individual comparison of the biograph vision quadra with the biograph vision pet/ct," *European journal of nuclear medicine and molecular imaging*, vol. 48, pp. 2395–2404, 2021.

- [13] K. Shibuya, H. Saito, H. Tashima, and T. Yamaya, "Using inverse laplace transform in positronium lifetime imaging," *Physics in Medicine & Biology*, vol. 67, no. 2, p. 025009, 2022.
- [14] J. Qi and B. Huang, "Positronium lifetime image reconstruction for tof PET," *IEEE Transactions on Medical Imaging*, 2022.
- [15] H.-H. Huang, Z. Zhu, S. Boopasiri, Z. Chen, S. Pang, and C.-M. Kao, "A statistical reconstruction algorithm for positronium lifetime imaging using time-of-flight positron emission tomography," 2023.
- [16] B. Huang, Z. Wang, X. Zeng, A. Goldan, and J. Qi, "High-resolution positronium lifetime imaging of extended heterogeneous biological samples," in *2023 IEEE Nuclear Science Symposium, Medical Imaging Conference and International Symposium on Room-Temperature Semiconductor Detectors (NSS MIC RTSD)*. IEEE, 2023, pp. 1–1.
- [17] R. Y. Shopa and K. Dulski, "Positronium imaging in j-pet with an iterative activity reconstruction and a multi-stage fitting algorithm," *Bio-Algorithms and Med-Systems*, vol. 19, no. 1, 2023.
- [18] Z. Chen, L. An, C.-M. Kao, and H.-H. Huang, "The properties of the positronium lifetime image reconstruction based on maximum likelihood estimation," *Bio-Algorithms and Med-Systems*, vol. 19, no. 1, 2023.
- [19] P. Virtanen, R. Gommers, T. E. Oliphant, M. Haberland, T. Reddy, D. Cournapeau, E. Burovski, P. Peterson, W. Weckesser, J. Bright, S. J. van der Walt, M. Brett, J. Wilson, K. J. Millman, N. Mayorov, A. R. J. Nelson, E. Jones, R. Kern, E. Larson, C. J. Carey, Í. Polat, Y. Feng, E. W. Moore, J. VanderPlas, D. Laxalde, J. Perktold, R. Cimrman, I. Henriksen, E. A. Quintero, C. R. Harris, A. M. Archibald, A. H. Ribeiro, F. Pedregosa, P. van Mulbregt, and SciPy 1.0 Contributors, "SciPy 1.0: Fundamental Algorithms for Scientific Computing in Python," *Nature Methods*, vol. 17, pp. 261–272, 2020.
- [20] L. Jødal, C. L. Loirec, and C. Champion, "Positron range in pet imaging: non-conventional isotopes," *Physics in Medicine & Biology*, vol. 59, no. 23, p. 7419, nov 2014. [Online]. Available: <https://dx.doi.org/10.1088/0031-9155/59/23/7419>
- [21] T. Matulewicz, "Radioactive nuclei for β^+ γ PET and theranostics: selected candidates," *Bio-Algorithms and Med-Systems*, vol. 17, no. 4, pp. 235–239, 2021.
- [22] J. Choiński and M. Łyczko, "Prospects for the production of radioisotopes and radiobioconjugates for theranostics," *Bio-Algorithms and Med-Systems*, vol. 17, no. 4, pp. 241–257, 2021.
- [23] S. Ferguson, H.-S. Jans, M. Wuest, T. Riauka, and F. Wuest, "Comparison of scandium-44 g with other pet radionuclides in pre-clinical pet phantom imaging," *EJNMMI physics*, vol. 6, no. 1, pp. 1–14, 2019.
- [24] K. Shibuya, E. Yoshida, F. Nishikido, T. Suzuki, T. Tsuda, N. Inadama, T. Yamaya, and H. Murayama, "Annihilation photon acollinearity in pet: volunteer and phantom fdg studies," *Physics in Medicine & Biology*, vol. 52, no. 17, p. 5249, 2007.
- [25] R. L. Siddon, "Fast calculation of the exact radiological path for a three-dimensional ct array," *Medical physics*, vol. 12, no. 2, pp. 252–255, 1985.
- [26] E. Grushka, "Characterization of exponentially modified gaussian peaks in chromatography," *Analytical chemistry*, vol. 44, no. 11, pp. 1733–1738, 1972.
- [27] H. M. Hudson and R. S. Larkin, "Accelerated image reconstruction using ordered subsets of projection data," *IEEE transactions on medical imaging*, vol. 13, no. 4, pp. 601–609, 1994.
- [28] L. Raczynski, W. Wiślicki, K. Klimaszewski, W. Krzemień, P. Kopka, P. Kowalski, R. Shopa, M. Bała, J. Chhokar, C. Curceanu *et al.*, "3d tof-pet image reconstruction using total variation regularization," *Physica Medica*, vol. 80, pp. 230–242, 2020.
- [29] Z. Chen, C.-M. Kao, H.-H. Huang, and L. An, "Enhancing positronium lifetime imaging through two-component reconstruction in time-of-flight positron emission tomography," 2024.

Mean (Standard deviation) of NMSE from the 10 simulation replicates						
Given	Regions	Proposed method	Exp-MLE	PS $\beta = 0$	PS $\beta = 5$	PS $\beta = 10$
f	Upper left	1.88×10^{-2} (1.93×10^{-3})	1.88×10^{-2} (1.78×10^{-3})	2.86×10^{-2} (3.35×10^{-3})	2.64×10^{-2} (2.70×10^{-3})	2.56×10^{-2} (2.99×10^{-3})
	Upper right	1.93×10^{-3} (3.70×10^{-4})	1.79×10^{-3} (2.67×10^{-4})	1.93×10^{-3} (3.48×10^{-4})	1.64×10^{-3} (3.62×10^{-4})	1.30×10^{-3} (3.23×10^{-4})
	Lower left	5.43×10^{-3} (7.64×10^{-4})	6.15×10^{-3} (8.90×10^{-4})	6.32×10^{-3} (8.33×10^{-4})	6.40×10^{-3} (8.83×10^{-4})	6.99×10^{-3} (8.87×10^{-4})
	Lower right	1.61×10^{-2} (9.54×10^{-4})	1.86×10^{-2} (1.04×10^{-3})	2.31×10^{-2} (8.67×10^{-4})	2.27×10^{-2} (1.22×10^{-3})	2.34×10^{-2} (1.33×10^{-3})
	Background	2.99×10^{-3} (1.77×10^{-4})	3.09×10^{-3} (1.82×10^{-4})	6.60×10^{-3} (1.95×10^{-4})	5.66×10^{-3} (2.07×10^{-4})	5.62×10^{-3} (1.98×10^{-4})
\hat{f}	Upper left	1.75×10^{-2} (1.78×10^{-3})	1.80×10^{-2} (3.03×10^{-3})	2.52×10^{-2} (3.25×10^{-3})	2.42×10^{-2} (3.62×10^{-3})	2.42×10^{-2} (3.37×10^{-3})
	Upper right	2.59×10^{-3} (5.23×10^{-4})	2.43×10^{-3} (4.87×10^{-4})	1.88×10^{-3} (3.46×10^{-4})	1.62×10^{-3} (3.66×10^{-4})	1.33×10^{-3} (3.07×10^{-4})
	Lower left	5.78×10^{-3} (8.52×10^{-4})	6.18×10^{-3} (8.53×10^{-4})	6.20×10^{-3} (8.02×10^{-4})	6.30×10^{-3} (9.49×10^{-4})	6.88×10^{-3} (9.49×10^{-4})
	Lower right	1.79×10^{-2} (1.26×10^{-3})	2.01×10^{-2} (1.13×10^{-3})	2.25×10^{-2} (8.93×10^{-4})	2.28×10^{-2} (2.58×10^{-3})	2.40×10^{-2} (2.70×10^{-3})
	Background	3.55×10^{-3} (1.68×10^{-4})	3.63×10^{-3} (1.59×10^{-4})	6.70×10^{-3} (2.14×10^{-4})	5.89×10^{-3} (2.29×10^{-4})	6.05×10^{-3} (2.06×10^{-4})

TABLE S1: Comparisons of NMSE using the five methods for Phantom 1 with f and \hat{f} . NMSE measurements of reconstructed images were taken across various regions including the upper left, upper right, lower left, lower right discs, and the background area defined by an ellipse excluding the four discs.